Available online at www.sciencedirect.com
SCIENCE DIRECT®
International Journal of Heat and Mass Transfer 48 (2005) 2662–2672
International Journal of HEAT and MASS TRANSFER
www.elsevier.com/locate/ijhmt

Constructal multi-scale structures with asymmetric heat sources of finite thickness

A.K. da Silva [a], S. Lorente [b], A. Bejan [a,*]

[a] Department of Mechanical Engineering and Materials Science, Duke University, Durham, NC 27708-0300, USA
[b] Laboratory for Materials and Durability of Constructions, National Institute of Applied Sciences (INSA), 135 Avenue de Rangueil, Toulouse 31077, France

Received 20 December 2004; received in revised form 31 January 2005
Available online 29 March 2005

Abstract

This paper details the generation of multi-scale flow structure in a package with heat sources. The model is based on abandoning two common assumptions (1) the assumption that there are many channels (components) in the package, which is traditionally made to exploit simplifications due to symmetry, and (2) the assumption that the heat-generating components have negligible thickness. Numerical simulations document the flow stagnation and separation generated by blunt heat sources, and the effect of these flow phenomena on the optimized internal flow structure. The effect of asymmetric thermal boundary conditions on the optimal spacing between heat-generating plates is significant. If the package has some channels with symmetric boundary conditions, and some with asymmetric boundary conditions, then the optimal structure has multiple spacings. The effect of freedom on design performance is documented by optimizing competing configurations that have different numbers of degrees of freedom.

Keywords: Constructal; Multi-scale; Optimal spacings; Discrete heat sources; Forced convection; Heatlines

1. Introduction

An emerging body of work [1–13] draws attention to the link between the maximization of the heat transfer rate packed into a fixed volume and the development of the internal structure of the package through which the coolant flows. This link represents a most fundamental optimization opportunity, which is applicable not only to the cooling of heat-generating packages but to flow structures in general. Spacings between solid parts must be sized in an optimal way, which is tailored to the intensity of the flow regime—tighter spacings where flows are faster. Spacings must be distributed in a certain way (non-uniformly) through a given volume—tighter spacings near the frontal region of the package. These features continue to hold as the size of the package decreases to dimensions so small that slender channels and boundary layers disappear, and the flow structure becomes a 'designed porous medium' [1,14].

In summary, the link between the maximization of heat transfer density and geometry is an invitation to the discovery of flow architecture. The generation of flow configuration is the mechanism through which the heat transfer device achieves its global objective. This

* Corresponding author. Tel.: +1 919 660 5309; fax: +1 919 660 8963.
E-mail address: dalford@duke.edu (A. Bejan).

0017-9310/$ - see front matter © 2005 Elsevier Ltd. All rights reserved.
doi:10.1016/j.ijheatmasstransfer.2005.01.028

Nomenclature

Be	pressure difference number, $\Delta P \cdot L^2/\mu\alpha$
C	global thermal conductance, Eq. (12)
c_P	specific heat at constant pressure, J kg^{-1} K^{-1}
dD	spacing used for the finite difference approximation, m
D	wall-to-wall spacing, m
H	heat function, W m^{-1}
k	thermal conductivity, W m^{-1} K^{-1}
L_d	extended inflow length, m
L_u	extended outflow length, m
P	pressure, Pa
Pr	Prandtl number
q'	heat transfer rate per unit length, W m^{-1}
q''_0	heat flux, W m^{-2}
R	residual vector
Re	Reynolds number
t	heat source thickness, m
T_{max}	peak wall temperature, K
T_0	inlet fluid temperature, K
u	horizontal velocity component, m s^{-1}
u	solutions vector
v	vertical velocity component, m s^{-1}
x, y	Cartesian coordinates, m

Greek symbols

α	thermal diffusivity, m^2 s^{-1}
ΔD	increment, m
ε	penalty parameter, m s kg^{-1}
μ	dynamic viscosity, Pa s
η	relative performance, Eq. (24)
ν	kinematic viscosity, m^2 s^{-1}
ρ	density, kg m^{-3}
τ	shear stress, N m^{-2}

Subscripts

H	high
it	iteration index
L	low
max	maximum
opt	optimum

Superscript

$\sim$	dimensionless variables

mechanism, or principle of geometry generation is now recognized as the constructal law [1,3].

The optimized spacings that have been uncovered so far were based on greatly simplifying assumptions, which made them tractable analytically. Chief among these is the assumption that there is a large number of solid components in a package, so large that it is sufficient to focus the analysis on a single spacing [7,15–20]. According to this assumption, the existence of walls that confine the package is neglected. Another frequent assumption is to neglect plate thicknesses in packages consisting of many parallel plates. This assumption simplifies the flow and the ensuing analysis, because streamlines remain essentially straight, and two-dimensional flow features are neglected (e.g., leading edge separation, flow upstreams of the package).

In this paper we study the optimization and generation of internal structure under considerably more realistic assumptions. We abandon the 'many plates' assumption and optimize the placement of very few heat-generating plates in a given space. The plates have thicknesses that cannot be neglected. Flows are two-dimensional, with secondary features such as separation downstream of the leading edges, and stagnation in front of every solid part. We focus on increasing Reynolds numbers, because secondary flows become stronger as the Reynolds number increases. We also document the effect of the confining walls, as well as the effect of asymmetry, for example, the case when the heat-generating component faces an adiabatic wall.

2. Mathematical formulation

Consider first the simplest configuration, which is the two-dimensional asymmetrically heated channel with one source, Fig. 1. The bottom wall is subject to a constant heat flux of strength q''_0. The height of the heat source is t. The channel is cooled by a single-phase fluid at T_0 which is forced into the channel by a specified pressure difference ($\Delta P = P_H - P_L$). The coolant is modeled as a Newtonian fluid and with constant properties. The dimensionless equations for the steady-state conservation of mass and momentum are

$$\frac{\partial \tilde{u}}{\partial \tilde{x}} + \frac{\partial \tilde{v}}{\partial \tilde{y}} = 0 \tag{1}$$

$$\frac{Be}{Pr}\left(\tilde{u}\frac{\partial \tilde{u}}{\partial \tilde{x}} + \tilde{v}\frac{\partial \tilde{u}}{\partial \tilde{y}}\right) = -\frac{\partial \tilde{P}}{\partial \tilde{x}} + \frac{\partial^2 \tilde{u}}{\partial \tilde{x}^2} + \frac{\partial^2 \tilde{u}}{\partial \tilde{y}^2} \tag{2}$$

$$\frac{Be}{Pr}\left(\tilde{u}\frac{\partial \tilde{v}}{\partial \tilde{x}} + \tilde{v}\frac{\partial \tilde{v}}{\partial \tilde{y}}\right) = -\frac{\partial \tilde{P}}{\partial \tilde{y}} + \frac{\partial^2 \tilde{v}}{\partial \tilde{x}^2} + \frac{\partial^2 \tilde{v}}{\partial \tilde{y}^2} \tag{3}$$

$$Be\left(\tilde{u}\frac{\partial \tilde{T}}{\partial \tilde{x}} + \tilde{v}\frac{\partial \tilde{T}}{\partial \tilde{y}}\right) = \frac{\partial^2 \tilde{T}}{\partial \tilde{x}^2} + \frac{\partial^2 \tilde{T}}{\partial \tilde{y}^2} \tag{4}$$

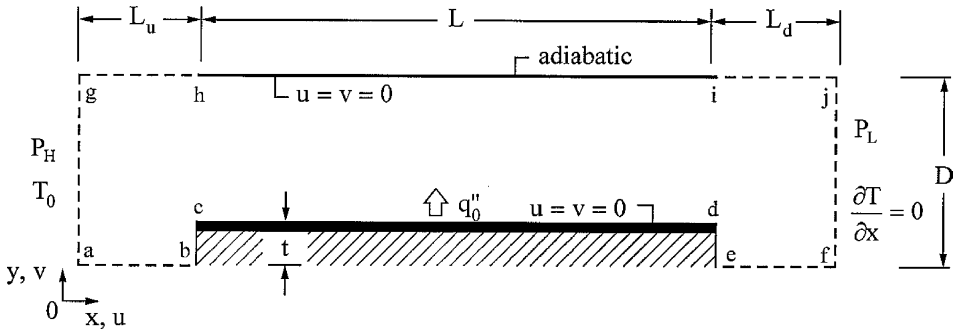

Fig. 1. Two dimensional channel heated asymmetrically.

where the dimensionless pressure difference is defined [21,22] as $Be = \Delta PL^2/\mu\alpha$. The non-dimensionalization of the governing equations is achieved by defining the variables

$$(\tilde{x}, \tilde{y}, \tilde{D}, \tilde{t}, \tilde{L}_u, \tilde{L}_d) = \frac{(x, y, D, t, L_u, L_d)}{L} \tag{5}$$

$$(\tilde{u}, \tilde{v}) = \frac{(u, v)}{(\Delta PL/\mu)} \tag{6}$$

$$\tilde{T} = \frac{T - T_0}{q''_0 L/k} \tag{7}$$

$$\tilde{P} = \frac{P}{\Delta P} \tag{8}$$

The origin of the Cartesian frame (x, y) is located in the bottom left corner of the computational domain, as shown in Fig. 1. The boundary conditions are

$$\begin{aligned}
&\overline{ab},\ \overline{gh},\ \overline{ef} \text{ and } \overline{ij}: \quad \tilde{v} = \frac{\partial \tilde{T}}{\partial \tilde{y}} = 0 \\
&\overline{ag}: \quad \tilde{P} = 1 \quad \text{and} \quad \tilde{T} = 0 \\
&\overline{fj}: \quad \tilde{P} = 0 \quad \text{and} \quad \frac{\partial \tilde{T}}{\partial \tilde{x}} = 0 \\
&\overline{hi}: \quad \tilde{u} = \tilde{v} = 0 \quad \text{and} \quad \frac{\partial \tilde{T}}{\partial \tilde{y}} = 0 \\
&\overline{cd}: \quad \tilde{u} = \tilde{v} = 0 \quad \text{and} \quad \tilde{q} = \frac{q''}{q''_0} = 1 \\
&\overline{bc} \text{ and } \overline{de}: \quad \tilde{u} = \tilde{v} = 0 \quad \text{and} \quad \frac{\partial \tilde{T}}{\partial \tilde{x}} = 0
\end{aligned} \tag{9}$$

The computational domain has three sections: the main channel of size $(D - t) \times L$ and the upstream and downstream extensions of sizes $D \times L_u$ and $D \times L_d$, respectively. The lengths of L_u and L_d were determined based on accuracy tests, by varying them and monitoring the changes in the hot spot temperature (T_{max}) for each geometric configuration that was simulated. Tests showed that T_{max} becomes insensitive to increments in L_u and L_d when both are larger than $0.5L$. These lengths are indicated in Fig. 1, but are not drawn to scale. The energy equation was not solved in the solid domain inside the heat source. Instead, $\tilde{q} = 1$ was applied on the horizontal surface, disregarding in this way the temperature gradient inside the heat source.

The numerical simulations were conducted using a code [23] based on the Galerkin finite elements method. The numerical domain was discretized non-uniformly using quadrilateral elements with nine nodes in each one. Refinement tests showed that the best grid is non-uniform in the y direction, with the smaller elements located close to the heated wall. The tests further showed that 101 nodes per unit of length L in the x direction and 201 per L in the y direction guarantee a grid accuracy in which the solution (T_{max}) changes by less than 1% when the mesh is doubled. This conclusion is valid throughout the range $10^5 \leqslant Be \leqslant 10^7$.

The conservation equations were solved in a simultaneous fully coupled manner. Because the flow is incompressible, we used the concept of artificial compressibility in order to determine the pressure uniquely. The pressure acts as a relaxation parameter to satisfy the continuity equation. Accordingly, the continuity equation is discarded and the pressure is eliminated from the momentum equations by using

$$P = -\frac{1}{\varepsilon}\left(\frac{\partial u}{\partial x} + \frac{\partial v}{\partial y}\right) \tag{10}$$

Here ε is the specified penalty factor, $\varepsilon = 10^{-8}$. Such a technique is unrealistic for unsteady flows, however, when the solution approaches the steady state, the left hand side term of Eq. (10) vanishes and the original continuity equation for incompressible fluids is recovered. The non-linear equations resulting from the finite element were solved in the range $10^5 \leqslant Be \leqslant 10^7$ by successive substitutions followed by the Newton–Raphson scheme. The convergence criterion was controlled by two parameters: the solution vector $\mathbf{u}_i$, and the residual vector $\mathbf{R}(\mathbf{u}_i)$,

$$\frac{||\mathbf{u}_{it} - \mathbf{u}_{it-1}||}{||\mathbf{u}_{it}||} \leqslant 0.0001 \quad \text{and} \quad \frac{||\mathbf{R}(\mathbf{u}_{it})||}{||\mathbf{R}_0||} \leqslant 0.0001 \tag{11}$$

where $\|\cdot\|$ is the Euclidean norm, 'it' is the iteration index, and $\mathbf{R}_0$ is a reference vector, typically $\mathbf{R}(\mathbf{u}_0)$.

3. Optimization procedure

For an asymmetrically heated channel, the plate-to-plate optimization opportunity consists of noticing that (i) larger D means smaller T_{max}, and (ii) small D means a compact channel. In the maximization of compactness, or heat transfer density, the figure of merit is the global conductance C defined as

$$C = \frac{q'L}{kD(T_{max} - T_0)} = \frac{1}{\widetilde{D}\widetilde{T}_{max}} \tag{12}$$

where q' is the total heat current, k is the fluid thermal conductivity, D is the plate-to-plate spacing, and $(T_{max} - T_0)$ is the peak excess temperature reached at any point on the bottom wall. In the C definition, D is an assumed geometric parameter, and T_{max} is an unknown to be determined numerically. The numerical search is for the configuration in which

$$\frac{\partial C}{\partial \widetilde{D}} = 0, \quad \text{at } \widetilde{D} = \widetilde{D}_{opt} \tag{13}$$

Newton's method was used in order to determine the optimal configurations. For fixed values of Be and Pr, one can approximate the objective function as a Taylor series for a given initial plate-to-plate spacing $\widetilde{D}^{\lambda}$,

$$\left.\frac{\partial C}{\partial \widetilde{D}}\right|_{\widetilde{D}^{\lambda}} \cong \left.\frac{\partial C}{\partial \widetilde{D}}\right|_{\widetilde{D}=\widetilde{D}_{opt}} + \Delta\widetilde{D}^{\lambda}\left.\frac{\partial^2 C}{\partial \widetilde{D}^2}\right|_{\widetilde{D}^{\lambda}} \tag{14}$$

Because the first term on the right hand side is zero when $\widetilde{D} = \widetilde{D}_{opt}$, one can estimate the increment $\Delta\widetilde{D}^{\lambda}$ that changes the configuration from the initial guess $\Delta\widetilde{D}^{\lambda}$ near the optimum,

$$\Delta\widetilde{D}^{\lambda} \approx \frac{\left.\frac{\partial C}{\partial \widetilde{D}}\right|_{\widetilde{D}^{\lambda}}}{\left.\frac{\partial^2 C}{\partial \widetilde{D}^2}\right|_{\widetilde{D}^{\lambda}}} \tag{15}$$

This suggests that the new configuration is

$$\widetilde{D}^{\lambda+1} \cong \widetilde{D}^{\lambda} \pm \Delta\widetilde{D}^{\lambda} \tag{16}$$

where the sign ± ensures that the new spacing $\widetilde{D}^{\lambda+1}$ converges toward the optimal solution.

The derivatives of Eq. (16) were determined by a second order central finite difference approximation. This means that for every guess $\widetilde{D}^{\lambda}$, two additional (neighboring) configurations were needed, $\widetilde{D}^{\lambda} + \Delta\widetilde{D}^{\lambda}$ and $\widetilde{D}^{\lambda} - \Delta\widetilde{D}^{\lambda}$. The neighboring configurations were located at $\Delta\widetilde{D} = 0.001$ for all the simulations that we performed. The optimization procedure described by Eqs. (15) and (16) was repeated until the convergence criterion $\Delta\widetilde{D}^{\lambda} \leqslant 0.0001$ was reached. The number of iterations needed in order to reach the specified convergence was between 4 and 6, depending on the initial guess for $\widetilde{D}^{\lambda}$.

Table 1
Comparison between numerical and theoretical results for optimal spacing and maximized thermal conductance

Be	$\frac{D_{opt}}{L}Be^{1/4}$		$\frac{2q'L}{kD_{opt}(T_{max}-T_0)}Be^{-1/2}$	
	Numerical	Theoretical [1,24]	Numerical	Theoretical [1,24]
10^5	3.03	3.2	0.391	0.4
10^6	3.05	3.2	0.394	0.4
10^7	3.12	3.2	0.394	0.4

The numerical results were further tested by comparing the theoretical and numerical optimal plate-to-plate and maximal global thermal conductance C obtained for a symmetrically heated channel. In this test case, the top and bottom walls that define the channel release a constant heat flux q''. Table 1 summarizes the comparison between the numerical and theoretical results. The theoretical results shown in Table 1 were obtained based on the intersection of asymptotes method [1,24]: the maximization of the global thermal conductance of a stack of horizontal plates with negligible thickness in forced convection. In this case, the optimal configuration emerges from the comparison of performance in two flow limits (i) fully developed flow ($D \to 0$), and (ii) boundary layer flow ($D \gg 2\delta$), where δ is the scale of the thickness of the thermal boundary layer. The theoretical results show that the optimal spacing $\widetilde{D}_{opt}$ must scale as $Be^{-1/4}$, and the maximized thermal conductance must scale as $Be^{1/2}$. The agreement is within 5.6% for the optimal plate-to-plate spacing, and 2.3% for the maximized global thermal conductance. The agreement improves as the pressure drop number increases.

4. Results

Fig. 2 shows how the selection of channel spacing affects the global thermal conductance of the configuration shown in Fig. 1. The effect of $\widetilde{D}$ on C is not symmetric about the optimal plate-to-plate spacing. The curve is much steeper when $\widetilde{D} < \widetilde{D}_{opt}$. On the other hand, as $\widetilde{D}$ increases beyond $\widetilde{D}_{opt}$, the maximum temperature T_{max} continues to drop because U_∞ increases ($U_\infty \sim D^{2/3}$, Ref. [24, p. 138]), where U_∞ is the mean velocity of the stream driven into the channel. This means that when $D > D_{opt}$, the reduction in global thermal performance (heat transfer density) is due to the increase in D, which overcomes the augmentation effect due to decreasing T_{max}.

Fig. 3 shows the variation of the actual spacing $(\widetilde{D}_{opt} - \widetilde{t})$ with the pressure drop number. The effect of the heat source thickness on the group $(\widetilde{D}_{opt} - \widetilde{t})$ is

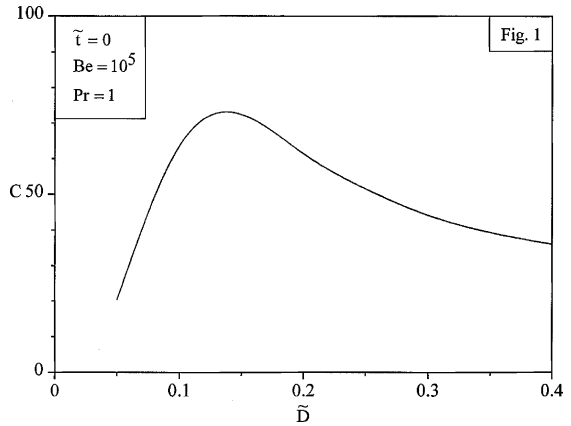

Fig. 2. The effect of the plate-to-plate spacing on the global thermal conductance.

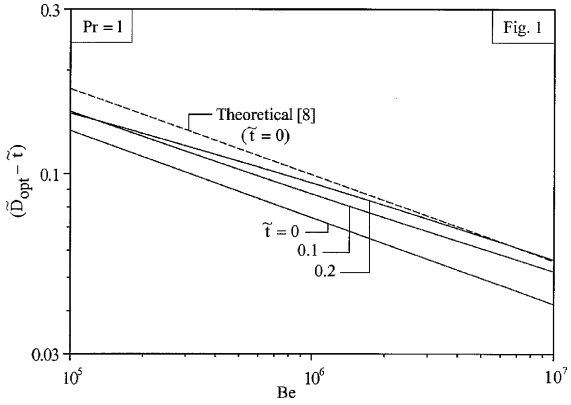

Fig. 3. The optimal channel spacing as a function of the heat source thickness.

noticeable, and all the curves are approximately parallel to $(\widetilde{D}_{opt} - \tilde{t}) \sim Be^{-1/4}$. In the same figure, the dashed line represents the optimal channel width determined theoretically [25], where $\widetilde{D}_{opt} Be^{1/4} = 3.14$. Nevertheless, two effects of $\tilde{t}$ on $\widetilde{D}_{opt}$ can be identified. Instead of the theoretical prediction [1,24], the more accurate correlation is of the type

$$\widetilde{D} - \tilde{t} \sim aBe^{-m} \tag{17}$$

where the dimensionless parameters a and m depend on $\tilde{t}$. In the range of $\tilde{t}$ studied, the factor a is smaller than 3.14, which is the value for an asymmetrically heated channel. In addition, a increases with $\tilde{t}$. The factor m decreases as $\tilde{t}$ increases.

Fig. 4 shows the effect of the heat source thickness on the maximized global thermal conductance. As can be expected, C_{max} decreases substantially as $\tilde{t}$ increases. This can be explained based on Fig. 3, which shows that the group $(\widetilde{D}_{opt} - \tilde{t})$ is essentially constant throughout

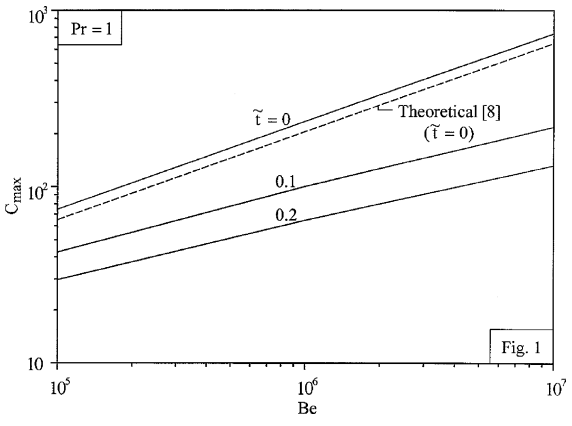

Fig. 4. The maximum global thermal performance that corresponds to the optimal plate-to-plate spacing.

the range $10^5 \leqslant Be \leqslant 10^7$. This means that the drop in performance is directly proportional to $\tilde{t}$. The dashed line represents the maximum theoretical global conductance for an asymmetrically heated channel with $\tilde{t} = 0$ [25], where $C_{max} = 0.205Be^{1/2}$. The agreement is good in an order of magnitude sense, with a maximum deviation of 13% between the theoretical prediction and the numerical results for $\tilde{t} = 0$.

Fig. 5 shows the streamlines and heatlines in the $(D - t) \times L$ region, for three different configurations $\widetilde{D} = 0.152$, 0.2 and 0.3, for $Be = 10^7$, $Pr = 1$ and $\tilde{t} = 0.1$. As $\widetilde{D}$ increases, flow separation and recirculation covers a larger section of the heat-generating surface, indicating the approach to turbulence. This conclusion is backed by the calculation of the local Reynolds number based on mean velocity u_m and transversal flow length $(D - t)$,

$$Re = \frac{u_m(D-t)}{\nu} = \tilde{u}_m(\widetilde{D} - \tilde{t})\frac{Be}{Pr} \tag{18}$$

By evaluating $\tilde{u}_m$ numerically, we find that the local Reynolds numbers for configuration (a), (b) and (c) are 270, 750 and 1370. This is consistent with the local Reynolds number criterion for transition to turbulence [1,24], which indicates that in channel flow at transition Re is on the order of 10^3. Another interesting conclusion derived from Fig. 5 is that, even at high pressure drop numbers ($Be \geqslant 10^7$), the appearance of separation is negligible when $(\widetilde{D} - \tilde{t}) \sim (\widetilde{D}_{opt} - \tilde{t})$. From Fig. 3 we know that $(\widetilde{D}_{opt} - \tilde{t}) = 0.05204$ or $\widetilde{D}_{opt} = 0.15204$ when $Be = 10^7$ and $\tilde{t} = 0.1$. For the exact same pressure drop (Be) and heat source height ($\tilde{t}$), Fig. 5b shows no sign of flow separation when $\widetilde{D} = 0.2$. This means that, for a fixed pumping power (Be) and heat source height ($\widetilde{D}$), separation will begin to occur when $(\widetilde{D} - \tilde{t}) \gg (\widetilde{D}_{opt} - \tilde{t})$. These conclusions are supported by the fact that the group $(\widetilde{D}_{opt} - \tilde{t})$ is reasonably constant for flows

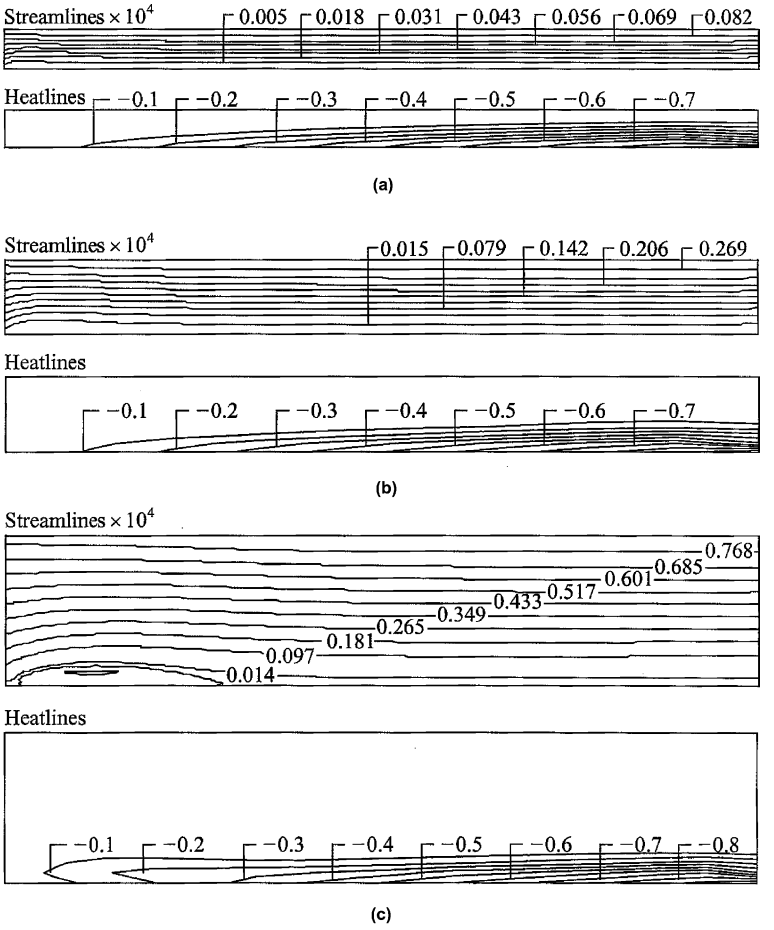

Fig. 5. Streamlines and heatlines showing the effect of channel spacing on flow separation and recirculation, when $Be = 10^7$, $Pr = 1$ and $\tilde{t} = 0.1$: (a) $\tilde{D}_{opt} = 0.152$; (b) $\tilde{D} = 0.2$; (c) $\tilde{D} = 0.3$.

driven by pressure differences in the range $10^5 \leqslant Be \leqslant 10^7$, and with heat source widths in the range $0 \leqslant \tilde{t} \leqslant 0.2$.

The heatlines presented in the lower frames of Fig. 5 were obtained by numerically solving the Poisson-type equation

$$\frac{\partial^2 \widetilde{H}}{\partial \tilde{x}^2} + \frac{\partial^2 \widetilde{H}}{\partial \tilde{y}^2} = Be\left[\frac{\partial(\tilde{u}\widetilde{T})}{\partial \tilde{y}} - \frac{\partial(\tilde{v}\widetilde{T})}{\partial \tilde{x}}\right] \tag{19}$$

where $\widetilde{H}$ is the dimensionless heatfunction [24] defined as $\widetilde{H} = H/q''_0 L$. The right hand side of Eq. (19) works as a source term. The field of heatlines was determined only in the $[(\widetilde{D} - \tilde{t}) \times \widetilde{L}]$ domain. The boundary conditions are $\mathrm{d}\widetilde{H}/\mathrm{d}\tilde{x} = -Be\tilde{v}\widetilde{T} + \mathrm{d}\widetilde{T}/\mathrm{d}\tilde{y}$ for the segments $\overline{ch}$ and $\overline{di}$ defined in Fig. 1, and $\mathrm{d}\widetilde{H}/\mathrm{d}\tilde{x} = \mathrm{d}\widetilde{T}/\mathrm{d}\tilde{y}$ for $\overline{cd}$ and $\overline{hi}$. The velocity and temperature fields were obtained with our finite elements package [23]. These fields were fed into a second order central finite difference C code, which determined the heatlines. The linear system solver used for Eq. (19) is similar to the preconditioned biconjugate gradient solver found in [26,27]. The convergence criterion was 10^{-6}. In Fig. 5a the heatlines come out of the heated wall in an equidistant pattern, and are pushed downstream by the flow. The heatlines of Fig. 5c show that the occurrence of flow separation distorts the heatlines upstream. A regular heatline pattern is established right after the end of the flow separation. Even though the effect of the separation is recognizable on the heat flow pattern for large values of D, the heatline pattern is well behaved when $D \sim D_{opt}$ (Fig. 5b). This is consistent with the negligible effect of flow separation on D_{opt}.

This conclusion is further supported by Fig. 6, which shows the local shear stress on the heated plate of the configuration shown in Fig. 1, for $\widetilde{D} = \widetilde{D}_{opt}$, 0.2, 0.3 and 0.4. The reattachment length is indicated with circles drawn at $\tilde{\tau} \approx 0$. According to Fig. 6, the reattachment length decreases with D, and it is approximately zero when $D = D_{opt}$.

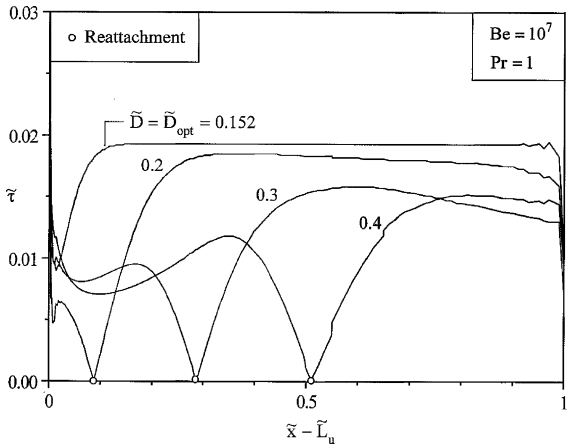

Fig. 6. The effect of the wall-to-wall spacing on the reattachment position.

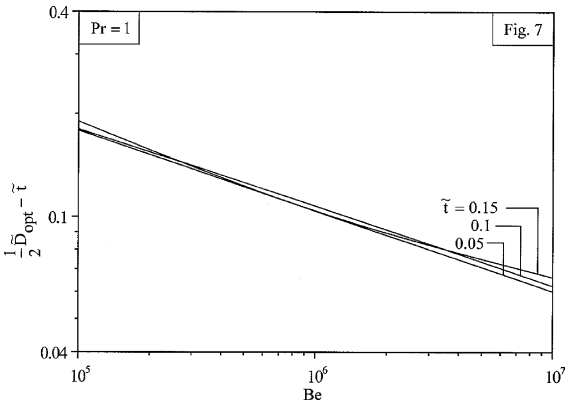

Fig. 8. The optimized spacing for the channels shown in Fig. 7.

A more complex configuration is shown in Fig. 7, where there are three heat-generating surfaces and two channels. The new numerical domain is defined by the same boundary conditions as in Fig. 1. More complex flow structures may also have secondary flow features when $D \gg D_{opt}$. However, the streamlines for the configuration of Fig. 7 are omitted due to convergence problems for values of $D \gg D_{opt}$. The reason for such numerical instabilities is that as D increases the package loses its 'slender look', and the local Reynolds number increases reaching into the turbulent range. The optimization procedure is the same as for the configuration of Fig. 1. The lone degree of freedom is D: the existence of an optimal spacing is expected on the same theoretical grounds as in Section 3.

Fig. 8 shows the behavior of the optimal channel spacing $(\tilde{D}_{opt}/2 - \tilde{t})$ versus the pressure drop number Be for the configuration of Fig. 7. Three values for the heat source thickness were considered. The collapse of the three curves shows that the effect of the thickness $\tilde{t}$ on the optimized spacing is minimal. This means that the optimized spacing is robust with respect to variations in source thickness. Another feature of robustness follows from the observation that the transversal flow length of Fig. 7 is almost equal to the transversal flow length of Fig. 1,

$$(\tilde{D}_{opt}/2 - \tilde{t})_{Fig.7} \sim (\tilde{D}_{opt} - \tilde{t})_{Fig.1} \tag{20}$$

Fig. 9 shows the maximized thermal performance of the configuration of Fig. 7 versus the pressure drop number. The figure of merit given by Eq. (12) still holds for the channel with three sources (Fig. 7), however, in Fig. 7 the hot surface has the length $3L$, and the maximum global thermal conductance is

$$C_{max} = \frac{3q'L}{kD_{opt}(T_{max} - T_0)} = \frac{3}{\tilde{D}_{opt}\tilde{T}_{max}} \tag{21}$$

The detrimental effect of $\tilde{t}$ on C_{max}, which was observed in Fig. 1, is also present in configurations with more than one heat source, Fig. 7. Based on Eq. (20) and

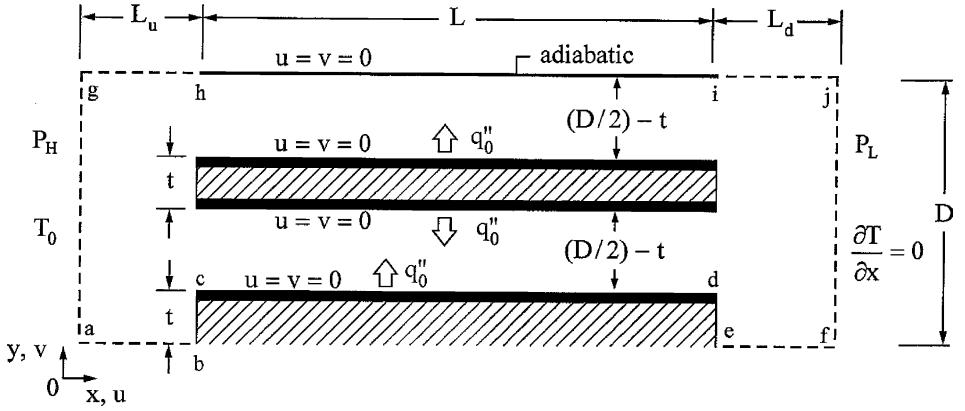

Fig. 7. Package with three hot surfaces and two channels.

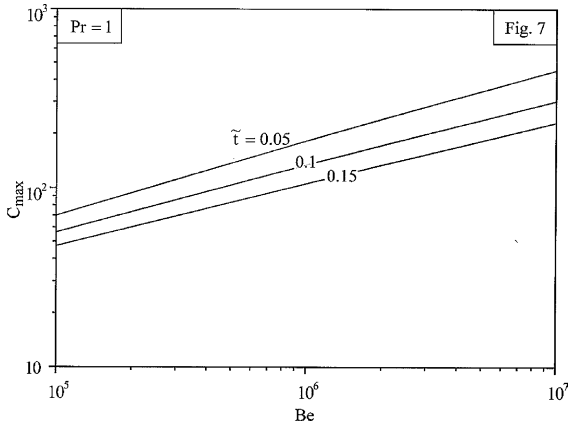

Fig. 9. The maximized global thermal conductance for the configuration shown in Fig. 7.

Fig. 8, which shows the constancy on the transversal flow length regardless of the height of the heat source, we conclude that the reduction of the global thermal conductance C_{max} is roughly proportional to $\tilde{t}$.

Next, we add one more degree of freedom to the configuration shown in Fig. 7, and the objective becomes the maximization of the global thermal conductance C with respect to two independent channel widths, $\tilde{D}_1$ and $\tilde{D}_2$, where $\tilde{D} = (2\tilde{t} + \tilde{D}_1 + \tilde{D}_2)$ as shown in Fig. 10. The boundary conditions of Figs. 1 and 7 still hold, however, the optimization procedure does not. For configurations with two degrees $\tilde{D} = f(\tilde{D}_1, \tilde{D}_2)$, Eq. (14) becomes the Hessian matrix (i.e., the Jacobian of the derivatives $\partial C/\partial \tilde{D}_1$ and $\partial C/\partial \tilde{D}_2$)

$$\begin{bmatrix} \dfrac{\partial^2 C}{\partial \tilde{D}_1^2} & \dfrac{\partial^2 C}{\partial \tilde{D}_1 \partial \tilde{D}_2} \\ \dfrac{\partial^2 C}{\partial \tilde{D}_1 \partial \tilde{D}_2} & \dfrac{\partial^2 C}{\partial \tilde{D}_2^2} \end{bmatrix} \begin{bmatrix} \Delta \tilde{D}_1 \\ \Delta \tilde{D}_2 \end{bmatrix}_\lambda = \begin{bmatrix} \dfrac{\partial C}{\partial \tilde{D}_1} \\ \dfrac{\partial C}{\partial \tilde{D}_2} \end{bmatrix}_\lambda \tag{22}$$

From the solution of Eq. (22), one can determine the newest configuration

$$\begin{aligned} \tilde{D}_1^{\lambda+1} &= \tilde{D}_1^{\lambda} \pm \Delta \tilde{D}_1^{\lambda} \\ \tilde{D}_2^{\lambda+1} &= \tilde{D}_2^{\lambda} \pm \Delta \tilde{D}_2^{\lambda} \end{aligned} \tag{23}$$

The applicability of this method is conditioned to the existence of the inverse of the Hessian matrix. Even though Newton's method has a quadratic convergence, its functionality is directly related to the accuracy of the derivatives of Eq. (22). This means that for a second order central finite difference approximation, nine points are required per iteration. This procedure was compared with a nested loop optimization, in which the increment toward the optimal configuration is assumed, and not calculated as in Newton's method. The comparison showed that the nested loop converges faster (i.e., fewer simulations are needed for one optimal configuration), given the same initial guess for both methods. The reason is that we already have good initial guesses for $\tilde{D}_1$ (symmetrically heated channel) and $\tilde{D}_2$ (asymmetrically heated channel) from Table 1 and Fig. 3, respectively.

Fig. 11 shows the optimal widths (bold curves) for the upper asymmetrically heated channel and for the bottom symmetrically heated channel shown in Fig. 10. The dashed curves represent the optimal channel width determined theoretically [7,25] for $\tilde{t} = 0$, where $\tilde{D}_{opt}$ is equal to $3.2Be^{1/4}$ and $3.14Be^{1/4}$ for the upper and lower frames, respectively. Unlike the results of Fig. 8, where $\tilde{D}_1 = \tilde{D}_2 = (\tilde{D}_{opt}/2 - \tilde{t})$, Fig. 11 shows that $\tilde{D}_{1,opt}$ is slightly larger than $\tilde{D}_{2,opt}$. For a fixed pressure drop number (Be) and heat source height ($\tilde{t}$), $\tilde{D}_{1,opt}$ is on average about 23% larger than $\tilde{D}_{2,opt}$. This apparent discrepancy was not captured by the optimal channel width determined theoretically, which suggests that the $\tilde{D}_{1,opt}$ is only 2% larger than $\tilde{D}_{2,opt}$. Most important is the fact that both theoretical solutions agree reasonably

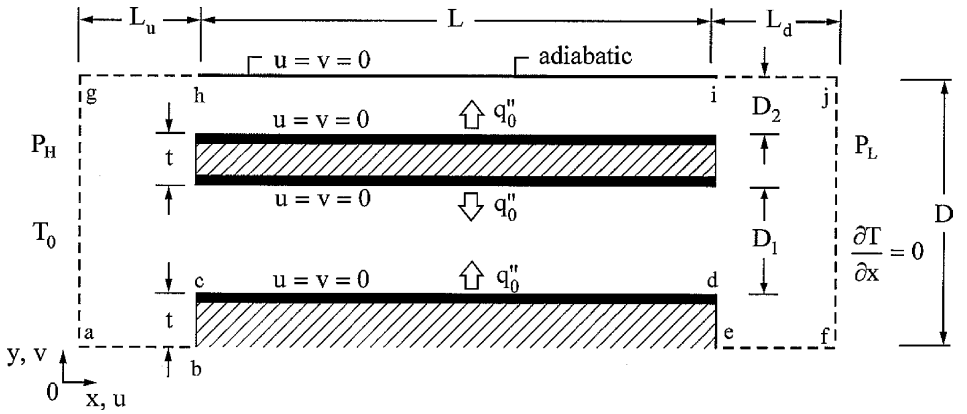

Fig. 10. Package with three heat sources and two channels with independent spacings.

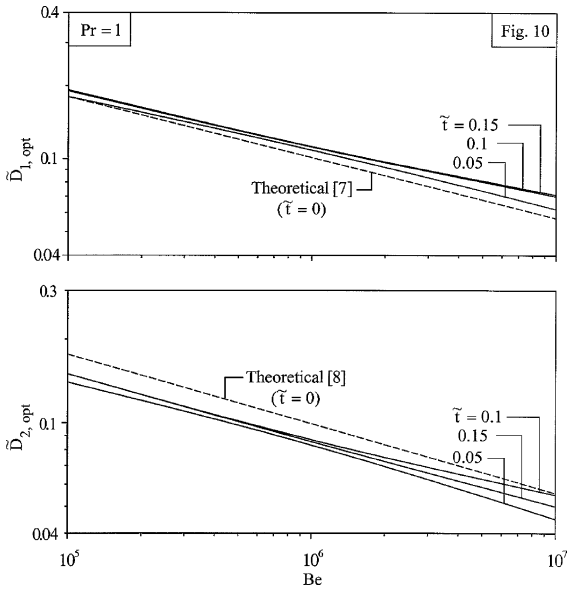

Fig. 11. The optimal spacings for the package shown in Fig. 10.

well with the numerical results. This confirms the robustness of the optimal spacing, even though the theoretical $\widetilde{D}_{1,\mathrm{opt}}$ and $\widetilde{D}_{2,\mathrm{opt}}$ were obtained in the limit where the hot blades have zero thickness.

Fig. 12 shows the maximized global conductance of Eq. (21), which is labeled C_{2m} in reference to the two degrees of freedom $(\widetilde{D}_1, \widetilde{D}_2)$. Like the behavior shown in Figs. 4 and 8, the heat source height $(\tilde{t})$ has a detrimental effect on the thermal performance of the configuration of Fig. 10. The reduction of performance is roughly proportional to $\tilde{t}$, because $\widetilde{D}_{1,\mathrm{opt}}$ and $\widetilde{D}_{2,\mathrm{opt}}$ are basically insensitive to changes in $\tilde{t}$.

Fig. 13 shows the relative performance (η) of the configurations presented in Figs. 7 and 10, where η is defined as

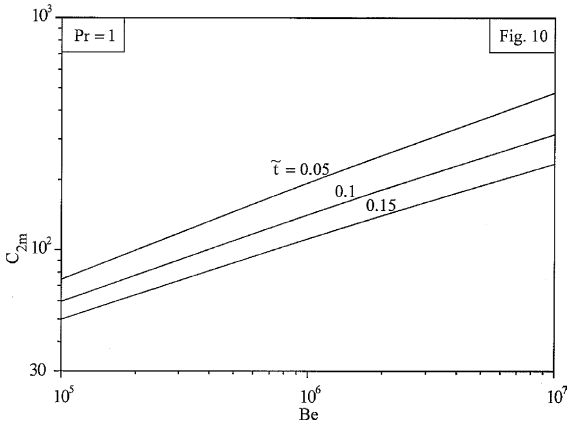

Fig. 12. The maximized global thermal performance of the package shown in Fig. 10.

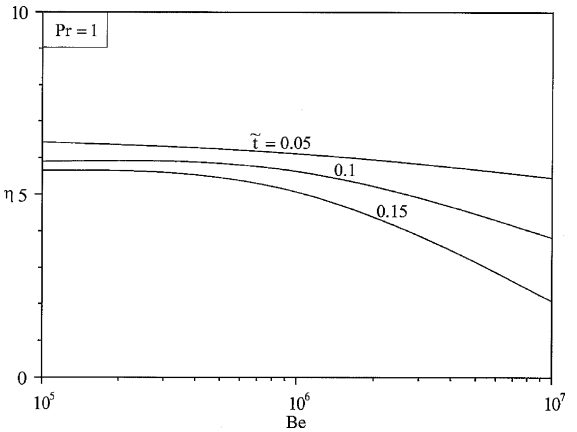

Fig. 13. The comparison of the relative performance of the packages shown in Figs. 7 and 10.

$$\eta = 100 \times \left| \frac{C_{2m,\mathrm{Fig.10}} - C_{\max,\mathrm{Fig.7}}}{C_{\max,\mathrm{Fig.7}}} \right| \tag{24}$$

The configuration with more degrees of freedom (Fig. 10) performs within 2–6.5% better than its simpler counterpart (Fig. 7). In conclusion, more freedom is good for global performance [3]. The same figure shows that the difference in performance between these two configurations reduces as *Be* increases.

5. Conclusions

In this paper we employed a more realistic numerical model to study the optimization of internal spacings in packages with heat-generating plates in forced convection. The model was based on relaxing two of the classical assumptions that modelers of parallel-plates packages make. First, we did not assume that the thickness of a heat-generating plate is negligible. The numerical results showed that the effect of finite plate thickness is to generate secondary flow features such as stagnation, separation and recirculation. These flow features have an effect on the optimized plate-to-plate spacings, however, this effect does not change the order of magnitude of the results.

The second classical assumption that we discarded is that the package contains a very large number of plates. The symmetry (repeatability of the channel flow field) that was the centerpiece of past numerical studies, was replaced in the present work by the need to simulate the entire (asymmetric) flow field through the package and its immediate vicinity. Our results show that when there are very few plates in the package, and when some of the plate surfaces are adiabatic, there is more than one optimal internal length scale. The optimized package is a multi-flow structure with multiple scales the sizes

and positions of which are optimized. Flow structures with multiple scales that are distributed optimally (hence non-uniformly) are encountered elsewhere in constructal design, for example in tree-shaped flow architectures [1–3,28–32].

The global performance of the package increases as the number of optimized dimensions (degrees of freedom) increases. Diminishing returns occur in the direction of higher optimized complexity. For example, the configuration in which two features can be optimized (D_1 and D_2 in Fig. 10) has a global performance that is 2–6.5% higher than in an optimized configuration with just one degree of freedom (Fig. 7).

Future work may extend the present study to heat transfer package models with even higher levels of complexity and realism. Good candidates are packages with larger numbers of components and asymmetric surface heating conditions, three-dimensional flow simulations that account for all the walls that confine the package, and the finite thermal conductivity of the parts that generate heat. Another aspect that deserves future study is the robustness of this class of optimized structures, for example, a comparison can be made between the maximized performance of structures with optimized multiple scales, and the performance of corresponding structures built with a single spacing based on existing results (e.g., Ref. [1]). If the difference is not great, then the optimized complex flow structure is robust, and it promises to perform close to the highest level even if not every single degree of freedom is exploited during the development of the flow architecture.

Acknowledgements

A.K. da Silva's work was fully supported by the Brazilian Research Council–CNPq under the Doctoral scholarship no. 200021/01-0. The authors also want to thank Prof. L. Gosselin (Université Laval, Québec, Canada) for his comments and suggestions on the numerical work.

References

[1] A. Bejan, I. Dincer, S. Lorente, A.F. Miguel, A.H. Reis, Porous and Complex Flow Structures in Modern Technologies, Springer-Verlag, New York, 2004.
[2] A. Bejan, Shape and Structure, from Engineering to Nature, Cambridge University Press, Cambridge, UK, 2000.
[3] A. Bejan, S. Lorente, The constructal law and the thermodynamics of flow systems with configuration, Int. J. Heat Mass Transfer 47 (2004) 3203–3214.
[4] K. Ogiso, Assessment of overall cooling performance in thermal design of electronics based on thermodynamics, J. Heat Transfer 123 (2001) 999–1005.
[5] J.R. Culham, Y.S. Muzychka, Optimization of plate fin heat sinks using entropy generation minimization, IEEE Trans. Compon. Pack. Technol. 24 (2001) 159–165.
[6] T. Furukawa, W.J. Yang, Thermal optimization of channel flows with discrete heating sections, J. Non-Equilib. Thermodyn. 28 (2003) 299–310.
[7] A. Bejan, E. Sciubba, The optimal spacing of parallel plates cooled by forced convection, Int. Heat Mass Transfer 35 (1992) 3259–3264.
[8] A. Bejan, Y. Fautrelle, Constructal multi-scale structure for maximal heat transfer density, Acta Mech. 163 (2003) 39–49.
[9] A.K. da Silva, S. Lorente, A. Bejan, Optimal distribution of discrete heat sources on a wall with natural convection, Int. J. Heat Mass Transfer 47 (2004) 203–214.
[10] A.K. da Silva, S. Lorente, A. Bejan, Optimal distribution of discrete heat sources on a plate with laminar forced convection, Int. J. Heat Mass Transfer 47 (2004) 2139–2148.
[11] A.K. da Silva, A. Bejan, S. Lorente, Maximal heat transfer density in vertical morphing channels with natural convection, Numer. Heat Transfer, Part A 35 (2004) 135–152.
[12] T. Bello-Ochende, A. Bejan, Maximal heat transfer density: plates with multiple lengths in forced convection, Int. J. Therm. Sci. 43 (2004) 1181–1186.
[13] A.K. da Silva, A. Bejan, Constructal multi-scale structure for maximal heat transfer density in natural convection, Int. J. Heat Fluid Flow 26 (2005) 34–44.
[14] A. Bejan, Designed porous media: maximal heat transfer density at decreasing length scales, Int. J. Heat Mass Transfer 47 (2004) 3073–3083.
[15] H.J. Sung, S.Y. Kim, J.M. Hyun, Forced convection from an isolated heat source in a channel with porous medium, Int. J. Heat Fluid Flow 16 (1995) 527–535.
[16] G.P. Xu, C.P. Tso, K.W. Tou, A review on direct liquid cooling channel flow with single-phase for electronic systems, J. Electron. Manuf. 6 (1996) 115–125.
[17] K.W. Tou, G.P. Xu, C.P. Tso, Direct liquid cooling of electronic chips by single-phase forced convection of FC-72, Exp. Heat Transfer 11 (1998) 121–134.
[18] D. Angirasa, G.P. Peterson, Forced convection heat transfer augmentation in a channel with a localized heat source using fibrous materials, J. Electron. Pack. 121 (1999) 1–7.
[19] C.P. Tso, G.P. Xu, K.W. Tou, An experimental study and forced convection heat transfer from flush-mounted discrete heat sources, J. Heat Transfer 121 (1999) 326–332.
[20] M. Iyengar, A. Bar-Cohen, Design for manufacturability of SISE parallel plate forced convection heat sinks, IEEE Trans. Compon. Pack. Technol. 24 (2001) 150–158.
[21] S. Bhattacharjee, W.L. Grosshandler, The formation of a wall jet near a high temperature wall under microgravity environment, ASME HTD 96 (1988) 711–716.
[22] S. Petrescu, Comments on the optimal spacing of parallel plates cooled by forced convection, Int. J. Heat Mass Transfer 37 (1994) 1283.
[23] FIDAP Manual, Fluid Dynamics International, Inc., Evanston, IL, 1998.
[24] A. Bejan, Convection Heat Transfer, third ed., Wiley, New York, 2004.
[25] A. Bejan, Al.M. Morega, S.W. Lee, S.J. Kim, The cooling of a heat-generating board inside a parallel-plate channel, Int. J. Heat Fluid Flow 14 (1993) 170–176.

[26] L.E. Howle, Lecture notes, Course ME 229—Computational Heat Transfer and Fluid Dynamics, Mechanical Engineering and Materials Science Department, Duke University.
[27] W.H. Press, S.A. Teukolsky, W.T. Vetterling, B.P. Flannery, Numerical Recipes in C—The Art of Scientific Computing, second ed., Cambridge University Press, New York, 1992.
[28] W. Wechsatol, S. Lorente, A. Bejan, Optimal tree-shaped networks for fluid flow in a disc-shaped body, Int. J. Heat Mass Transfer 45 (2002) 4911–4924.
[29] S. Lorente, W. Wechsatol, A. Bejan, Tree-shaped flow structures designed by minimizing path lengths, Int. J. Heat Mass Transfer 45 (2002) 3299–3312.
[30] W. Wechsatol, S. Lorente, A. Bejan, Dendritic convection on a disc, Int. J. Heat Mass Transfer 46 (2003) 4381–4391.
[31] L.A.O. Rocha, S. Lorente, A. Bejan, Constructal design for cooling a disc-shaped area by conduction, Int. J. Heat Mass Transfer 45 (2002) 1643–1652.
[32] A.K. da Silva, S. Lorente, A. Bejan, Constructal multi-scale tree-shaped heat exchangers, J. Appl. Phys. 96 (3) (2004) 1709–1718.